

MULTI-OBJECTIVE SHAPE OPTIMIZATION OF A LAUNCH VEHICLE FAIRING ACROSS MULTIPLE FLOW REGIMES

A. Petrillo[1], D. Palma[1], L. Pirillo[1], P. P. Ciottoli[1], M. Bernardini[1] & F. Stella[1]

[1]Sapienza University of Rome, via Eudossiana 18, Rome (RM), 00184, Italy

Abstract

This study presents a multi-objective shape optimization framework for a launch vehicle payload fairing across multiple flow regimes. The approach integrates the modeFRONTIER platform with wall-resolved RANS CFD simulations in ANSYS Fluent, parameterizing the fairing geometry via a fifth-degree Bézier curve with four degrees of freedom. First, single-objective drag minimizations across different regimes are performed, revealing conflicting geometric requirements for different flight conditions. Then, a multi-objective optimization is performed in the supersonic regime, simultaneously minimizing aerodynamic drag and peak surface heat flux, and identifying a well-balanced intermediate configuration on the Pareto front. Finally, a cross-regime evaluation demonstrates that single-point optimized shapes underperform outside their design conditions. In this context, the supersonic intermediate configuration optimized for both drag and heat fluxes proves to be a robust compromise, effectively balancing thermal loads while mitigating transonic drag penalties. These findings highlight the limitations of single-point optimization and underscore the necessity of a trajectory-based framework for robust launch vehicle design.

Keywords: Aerodynamics, Optimization, CFD, Fairing, Launcher

1. Introduction

Shape optimization has become a central topic in modern aerospace engineering, driven by the need to balance competing performance objectives while operating under increasingly demanding design constraints. Across a wide range of applications, optimal geometries must simultaneously address aerodynamic efficiency, structural integrity, thermal loads, and manufacturability, often across multiple operating conditions and flow regimes. The inherently multidisciplinary and multi-objective nature of these problems makes shape optimization a persistent and still open challenge.

Within this broader context, launch vehicle design represents a particularly demanding application. During atmospheric ascent, external aerodynamic shapes strongly influence both drag losses and aerothermal environments, with direct consequences on vehicle performance and payload safety. Payload fairings, in particular, must satisfy conflicting aerodynamic and thermal requirements over a wide Mach number range, making them suitable candidates for advanced multi-objective optimization methodologies.

CFD-based optimization techniques have been widely applied in aerospace engineering to address aerodynamic design problems under different operating conditions. Nassif et al. [1] investigated multi-point surrogate-based optimization strategies for hypersonic waveriders, emphasizing the importance of robust aerodynamic performance across multiple operating conditions. Similar multi-point optimization methodologies were explored by Kenway and Martins [2] for transonic aircraft wings, demonstrating the effectiveness of high-fidelity CFD-driven optimization frameworks in realistic aerodynamic environments. Multi-objective and multipoint optimization strategies were also investigated by Massaro et al. [3] in the context of rotor blade aerodynamics using surrogate-assisted optimization methods.

https://doi.org/10.71945/icas2026_0284

Fundamental aerodynamic drag minimization approaches were studied by Hicken and Zingg [4], who investigated induced-drag minimization for nonplanar geometries through Euler-based methodologies. Additional aerodynamic optimization studies have been performed across several engineering applications. Hashimoto et al. [5] investigated aerodynamic optimization techniques for high-wing aircraft configurations, while Yu et al. [6] explored shape optimization methodologies for high-speed train nose geometries with the aim of simultaneously reducing aerodynamic resistance and noise generation.

In the context of launch vehicle and high-speed aerospace applications, Colonno and Alonso [7] proposed an early multidisciplinary design optimization framework for launcher fairings, highlighting the relevance of system-level optimization approaches for external aerodynamic configurations. More recent studies focused specifically on launcher and fairing geometries under compressible flow conditions. Sunil et al. [8] investigated aerodynamic optimization of payload fairing boattail geometries for drag reduction, whereas Yin et al. [9] explored hypersonic vehicle optimization using advanced shape parameterization techniques. Shen et al. [10] further demonstrated the applicability of CFD-based optimization methodologies to high-speed fairing configurations. More recently, Della Monica and Bernardini [11] investigated CFD-driven optimization strategies for the external aerodynamics of a sounding rocket, confirming the growing importance of high fidelity aerodynamic optimization methodologies in launcher applications.

Despite these advances, most existing studies remain primarily focused on single operating conditions or specific flow regimes. As a consequence, the robustness of optimized fairing geometries across subsonic, transonic, and supersonic conditions remains relatively unexplored, particularly when both aerodynamic and aerothermal objectives are simultaneously considered.

In this context, the present work introduces a multi-objective shape optimization framework for the fairing of a launch vehicle prototype that explicitly targets the simultaneous minimization of aerodynamic drag and peak surface heat flux acting on the fairing. The work relies on the optimization platform modeFRONTIER, integrated with wall-resolved turbulent CFD simulations in ANSYS Fluent for the execution of the optimization process. Initially, a subsonic test case at Mach 0.5 and a transonic test case at Mach 0.81 are investigated, focusing on single-objective optimizations aimed at minimizing the fairing drag coefficient (C_d) under these specific flight conditions. Subsequently, a supersonic test case at Mach 1.8 is performed using a multi-objective approach to simultaneously minimize the drag coefficient and the peak surface heat flux acting on the fairing. This choice is motivated by the fact that the most critical conditions from an aerothermal design standpoint are typically encountered in the supersonic flight regime, where compressibility effects and aerodynamic heating become significantly more pronounced. Consequently, the inclusion of thermal constraints and heat flux minimization is considered particularly relevant under these operating conditions. Finally, a cross-regime evaluation of the selected regime-optimal configurations is performed to assess their aerodynamic and aerothermal robustness outside the flow regime in which they were originally optimized.

2. Methodology

2.1 Geometry parametrization

A conventional ogive-shaped launcher fairing geometry was selected as the baseline configuration for the present optimization study. Bézier curves are selected for geometric parametrization to provide an efficient design framework while minimizing the dimensionality of the design space [12]. This approach inherently ensures geometric smoothness, effectively filtering out irregular or unrealistic geometries during the aerodynamic optimization. The ogive shape is parameterized by a fifth-degree Bézier curve defined by six control points. This geometric framework is designed to maintain fixed cylindrical envelope dimensions to accommodate a defined satellite payload, while allowing controlled variation of the ogive profile. The first two and the last two points remain fixed, anchoring the curve at its boundaries; specifically, these end conditions constrain the curve to a vertical tangent at the nose and a horizontal tangent at the interface with the cylindrical section, ensuring smoothness and manufacturability. Consequently, the design space is characterized by four degrees of freedom (DOFs), represented by the Cartesian coordinates of the two mobile internal control points, as shown

in Figure 1.
It is worth underlining that the Bézier curve does not generally pass through the control points; instead, these points act as geometric attractors that influence the local curvature of the fairing profile. In particular, the tangent direction at the beginning and end of the curve is determined by the alignment of the first and last pairs of control points, while the two internal movable points progressively modify the curvature distribution along the ogive. As a result, smooth geometric variations can be obtained by simply adjusting the position of the control points, allowing the generation of a wide range of aerodynamic shapes while preserving continuity and manufacturability constraints. Each movable control point has a distinct influence on the resulting fairing geometry. Specifically, shifting Point A toward the left generates a blunter nose configuration, whereas moving it toward the right produces a sharper and more slender forebody. The vertical coordinates of both internal points primarily affect the overall fairing volume and internal payload capacity, with larger values leading to fuller geometries. In addition, translating Point B upstream extends the nearly horizontal portion of the profile close to the cylindrical section, thereby modifying the curvature transition between the ogive and the main body.

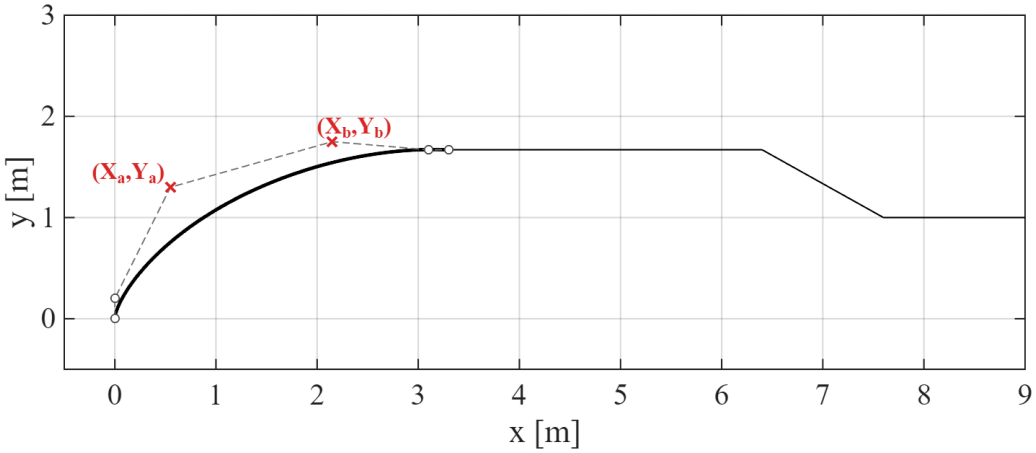


Figure 1 – Overview of design variables used in the optimization process.

Figure 2 illustrates various examples of geometries that can be obtained through this parameterization by varying the positions of the control points.

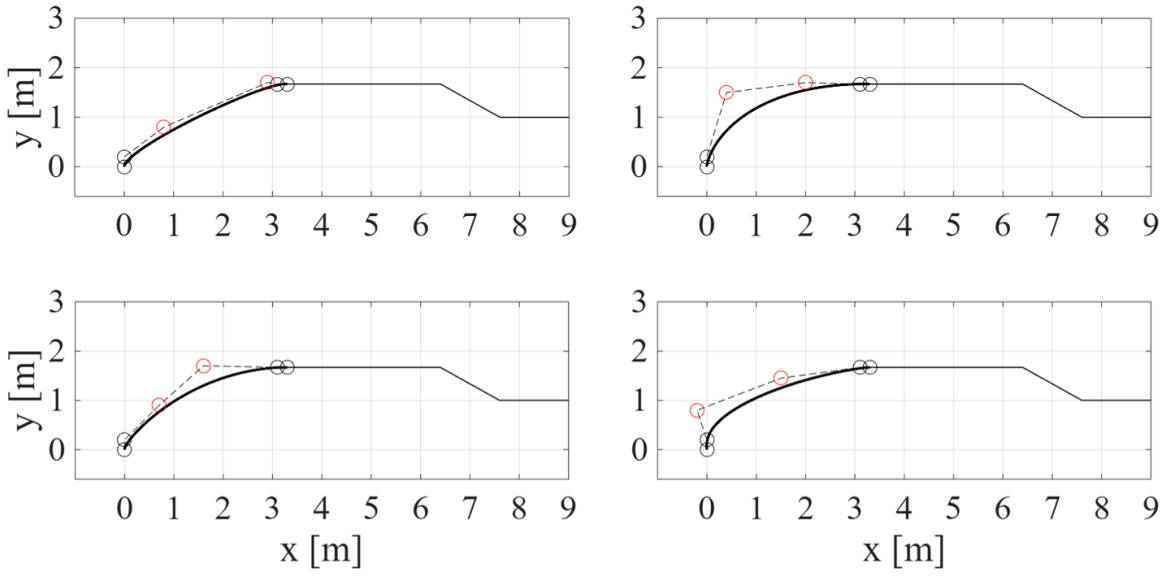


Figure 2 – Examples of alternative fairing profiles generated by varying internal control points.

The coordinates of the movable control points are constrained within predefined upper and lower bounds to prevent the generation of aerodynamically unfeasible shapes during the optimization process. The specific upper and lower bounds defined for each design variable are listed in Table 1:

Table 1 – Lower and upper bounds imposed on the design variables defining the movable Bézier control points.

Design Variable	Lower Bound	Upper Bound
x_A	-0.2	3.0
y_A	0.2	1.8
x_B	0.2	3.0
y_B	1.4	1.7

2.2 Optimization algorithm

The optimization task is addressed using a Bayesian Optimization (BO) framework, which is particularly well suited for scenarios involving the evaluation of expensive black-box functions. These algorithms are gradient-free and prove highly effective in locating global optima with a relatively small number of function evaluations. This efficiency is particularly advantageous in computationally intensive fields such as CFD, where each simulation represents a significant computational cost. The theoretical foundations and successful applications of these methods in CFD-based optimization have been demonstrated in previous studies [13, 14, 15, 16, 17], yet they are still not widely adopted in practical optimization tasks.

In BO, a stochastic process is introduced to construct a response surface model (RSM) of the objective function $y(x)$, which can be written as follows:

$$y(\boldsymbol{x}) = \mu + \varepsilon(\boldsymbol{x}). \tag{1}$$

The term $\varepsilon(\boldsymbol{x})$ is assumed to be a Gaussian stochastic process with zero mean and covariance function

$$k(\boldsymbol{x}_i, \boldsymbol{x}_j) = \sigma^2 Corr(\boldsymbol{x}_i, \boldsymbol{x}_j) = \sigma^2 exp\left[-\sum_{h=1}^{n} \theta_h |x_{i,h} - x_{j,h}|^{p_h}\right]. \tag{2}$$

The parameters μ, σ, θ_h and p_h are estimated by maximizing the likelihood function. Once these parameters are determined, the prediction of the function $y(\boldsymbol{x})$ at the point $\boldsymbol{x}^*$ and the mean squared error of the predictor can be computed using the following formulas:

$$\hat{y}(\boldsymbol{x}^*) = \hat{\mu} + \boldsymbol{r}^T \boldsymbol{R}^{-1}(\boldsymbol{y} - \mathbf{1}\hat{\mu}) \tag{3}$$

$$s^2(\boldsymbol{x}) = \hat{\sigma}^2 \left(1 - \boldsymbol{r}^T \boldsymbol{R}^{-1} \boldsymbol{r} + \frac{(1 - \mathbf{1}^T \boldsymbol{R}^{-1} \boldsymbol{r})^2}{\mathbf{1}^T \boldsymbol{R}^{-1} \mathbf{1}}\right) \tag{4}$$

where $\hat{\mu}$ and $\hat{\sigma}$ are the estimated mean and variance, $\boldsymbol{y}$ is the vector of values assumed by the objective function, R is the correlation matrix whose element (i, j) is given by $Corr(\boldsymbol{x}_i, \boldsymbol{x}_j)$, and r is a vector whose i-th element is $Corr(\boldsymbol{x}^*, \boldsymbol{x}_i)$.

Proposed by Jones et al., the Efficient Global Optimization (EGO) algorithm incorporates the previously described Gaussian Process as a surrogate model, utilizing the Expected Improvement (EI) criterion to guide the sampling process [18]. In the present work, a multi-objective version which adopts the Expected Hypervolume Improvement (EHVI) infill criterion [19] is implemented through modeFRONTIER. A Gaussian process is trained for each objective function $y_i(x)$, providing a mean $\mu_i(x)$ and a standard deviation $\sigma_i(x)$. These components are then used to compute the Lower Confidence Bound (LCB) for every candidate point x in the design space:

$$\boldsymbol{y}_{LCB}(\boldsymbol{x}) = \boldsymbol{\mu}(\boldsymbol{x}) - 2\boldsymbol{\sigma}(\boldsymbol{x}). \tag{5}$$

The selection of the next design point to be evaluated is then driven by the maximization of the function:

$$EHVI_{LCB}(\boldsymbol{x}) = max(HVI(P \cup \boldsymbol{y}_{LCB}(\boldsymbol{x})) - HVI(P), 0) \tag{6}$$

where HVI is the hypervolume indicator and $P = \{\boldsymbol{p}_1, ..., \boldsymbol{p}_n\}$ is the current Pareto front approximation. The initial database is determined using a Latin Hypercube Sampling (LHS) strategy to define the Design of Experiments (DOE). Unlike random sampling, LHS ensures a space-filling distribution of the initial points, providing a robust global representation of the design space with a limited number of samples [20].

2.3 Computational setup

The optimization framework is integrated with CFD simulations in ANSYS Fluent. Reynolds-Averaged Navier Stokes (RANS) equations for compressible flows are solved under the assumptions of a steady state flow and an ideal gas formulation. Simulations are performed at a zero angle of attack; consequently, the problem is modeled as a 2D axisymmetric flow, given the geometric symmetry of the fairing. A pressure-based solver with the coupled algorithm is selected to manage the pressure-velocity coupling, and a second order upwind scheme is employed for the discretization of convective terms. The turbulence model employed for the closure of RANS equations is the Shear Stress Transport (SST) k-ω model [21]. This two equation turbulence model utilizes a blending function to combine the accuracy of the k-ω formulation in the near wall region with the insensitivity of k-ω to freestream values. Concerning the boundary conditions, a pressure far field condition is applied at the external boundaries, where the free stream Mach number, static temperature, and static pressure are prescribed. The fairing surface is modeled as a no slip isothermal wall with a fixed temperature of 300 K.
The computational mesh employed for the simulations is shown in Figure 3.

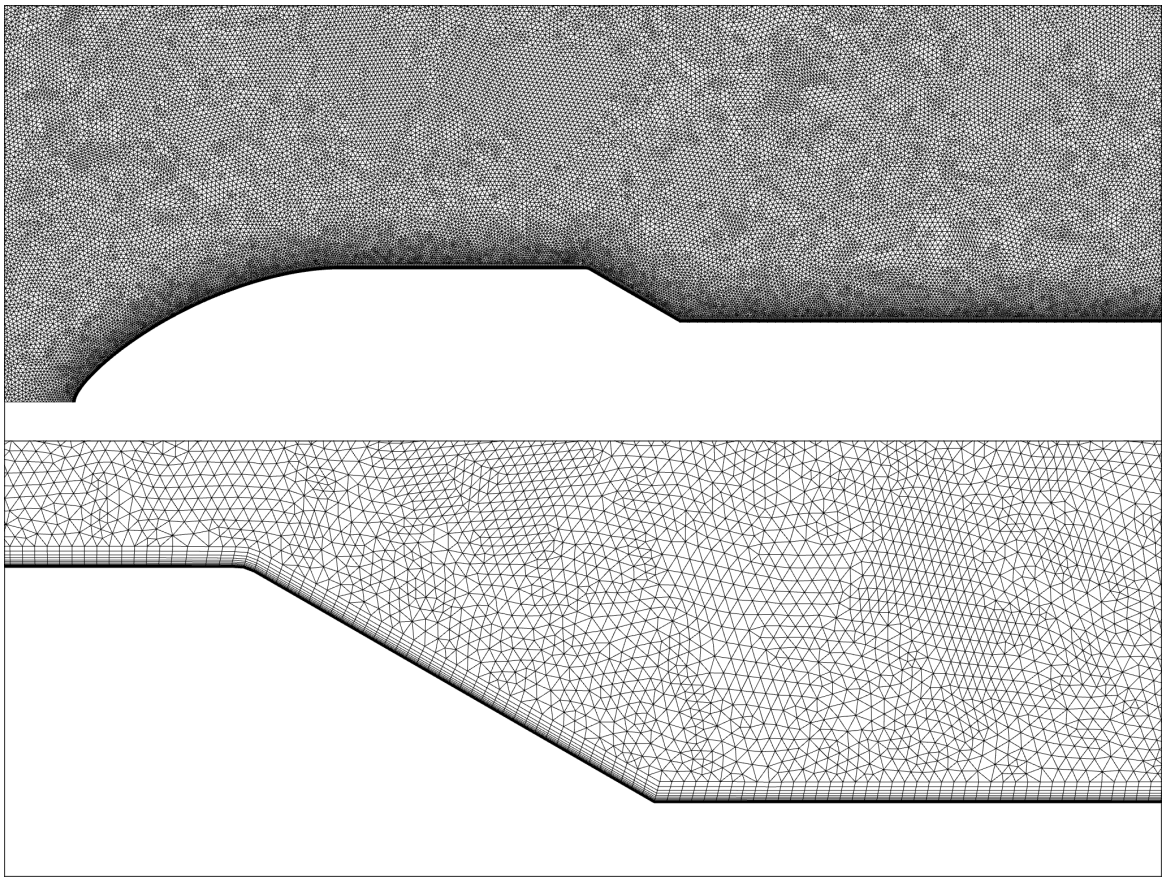


Figure 3 – Computational mesh overview (top) and detail of the inflation layers at the wall (bottom).

It consists of an unstructured grid with a structured inflation layer at the walls to resolve the boundary layer, ensuring a $y^+ \sim 1$. The total number of cells was determined through a mesh sensitivity analysis performed taking into account the supersonic case. The sensitivity procedure evaluates the C_d and the peak surface heat flux on the fairing. The results are shown in Table 2. Both the coarse and medium grids exhibit C_d values very close to those of the fine mesh. However, this is not the case

for the peak heat flux, where the coarse grid shows a deviation of 9.59%, compared to only 1.26% for the medium one. Since the variations of the medium mesh relative to the fine one are small for both quantities, the medium mesh was selected for the study as the best trade-off between numerical accuracy and computational efficiency.

Table 2 – Mesh sensitivity analysis evaluating drag and peak surface heat flux.

Mesh	**# cells**	**Peak Heat Flux [kW/m^2]**	**Drag coefficient [-]**
Coarse mesh	$3.5 \cdot 10^5$	48.5	5.579
Medium mesh	$5.7 \cdot 10^5$	54.3	5.588
Fine mesh	$8.2 \cdot 10^5$	53.6	5.603

The optimization process begins once all points of the initial random dataset generated through LHS have been evaluated through CFD simulations. Within this framework, each new candidate point for the global optimum search is determined by the infill criterion described in Section 2.2 and subsequently evaluated through a numerical simulation. The process continues until either convergence is achieved or a prescribed maximum number of simulations is reached.

3. Results

The results of the performed optimizations are presented and discussed in the following sections. First, Section 3.1 reports the outcomes of the two single-objective optimizations, which were aimed at minimizing aerodynamic drag in subsonic and transonic conditions, respectively. Subsequently, Section 3.2 presents the results of the multi-objective optimization conducted in the supersonic regime. Finally, in Section 3.3, the robustness of the obtained solutions is evaluated by testing the profiles in flow regimes different from those for which they were originally optimized.

3.1 Single-objective optimizations results

Both optimizations are carried out by evaluating 20 configurations in the DoE, and then evaluating 20 design points with the optimization algorithm. This number of evaluations is found to be sufficient for both subsonic and transonic cases to reach satisfactory convergence, as shown in Figure 4.

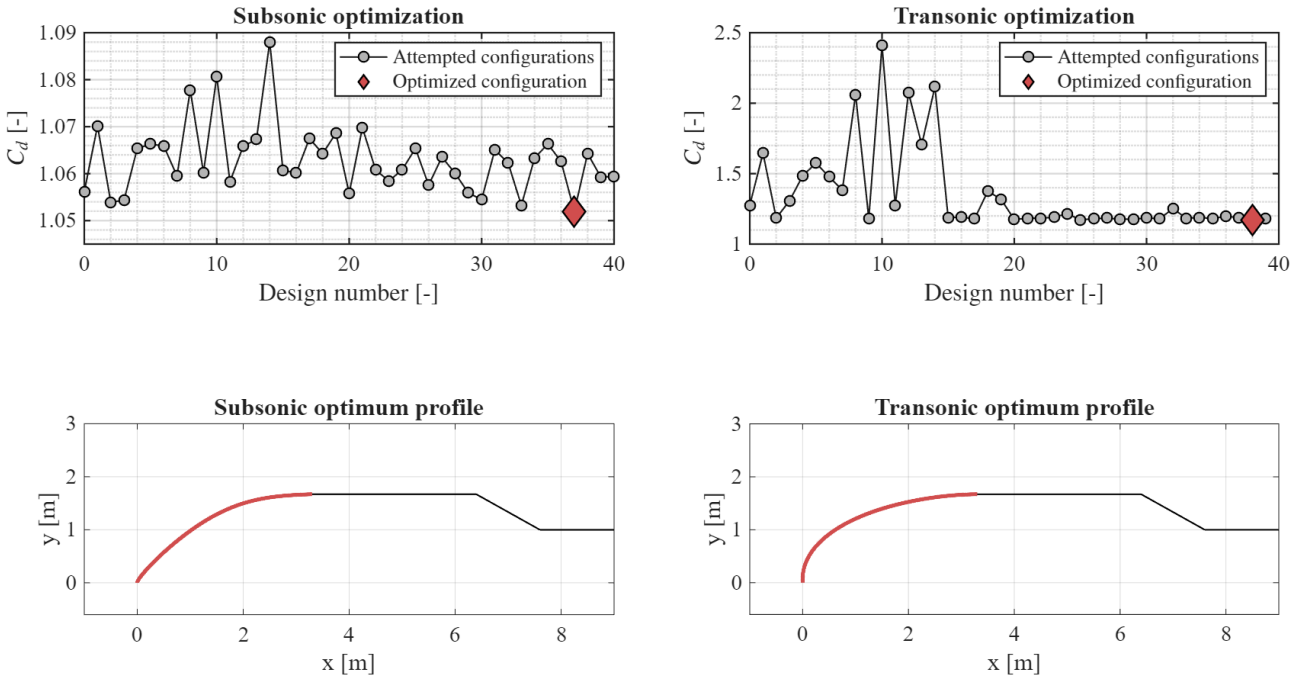


Figure 4 – From top left to bottom right: convergence history of the subsonic optimization process, convergence history of the transonic optimization process, optimized subsonic launcher profile, and optimized transonic launcher profile.

The ogive profiles corresponding to the optimum found with the optimization process are shown in the bottom part of Figure 4. The geometrical comparison reveals that the subsonic fairing exhibits a sharper profile, while the transonic configuration is characterized by a blunter and smoother contour. The aerodynamic effects of the selected profiles on the flow field are analyzed in Section 3.3, along with the cross-regime evaluation.

3.2 Multi-objective optimization results

The objective of the multi-objective optimization is the minimization of the aerodynamic drag and of the peak heat flux acting on the fairing surface. In this test case, 30 elements are generated for the DoE. Unlike single-objective optimization, the outcome of a multi-objective optimization is not a single optimal configuration, but rather a set of solutions forming the so-called Pareto front. Each configuration belonging to the Pareto front represents a different trade-off between the competing objectives, assigning a different relative importance to drag reduction and heat flux minimization. Consequently, improving one objective generally leads to a deterioration of the other. All the configurations lying on the Pareto front are considered optimal solutions, since none of them can improve one objective without penalizing the other. Therefore, the final selection of a specific configuration depends on

the particular mission requirements and on the relative importance assigned to aerodynamic performances or thermal load reduction. Following the optimization process, the extracted Pareto front is shown in Figure 5.

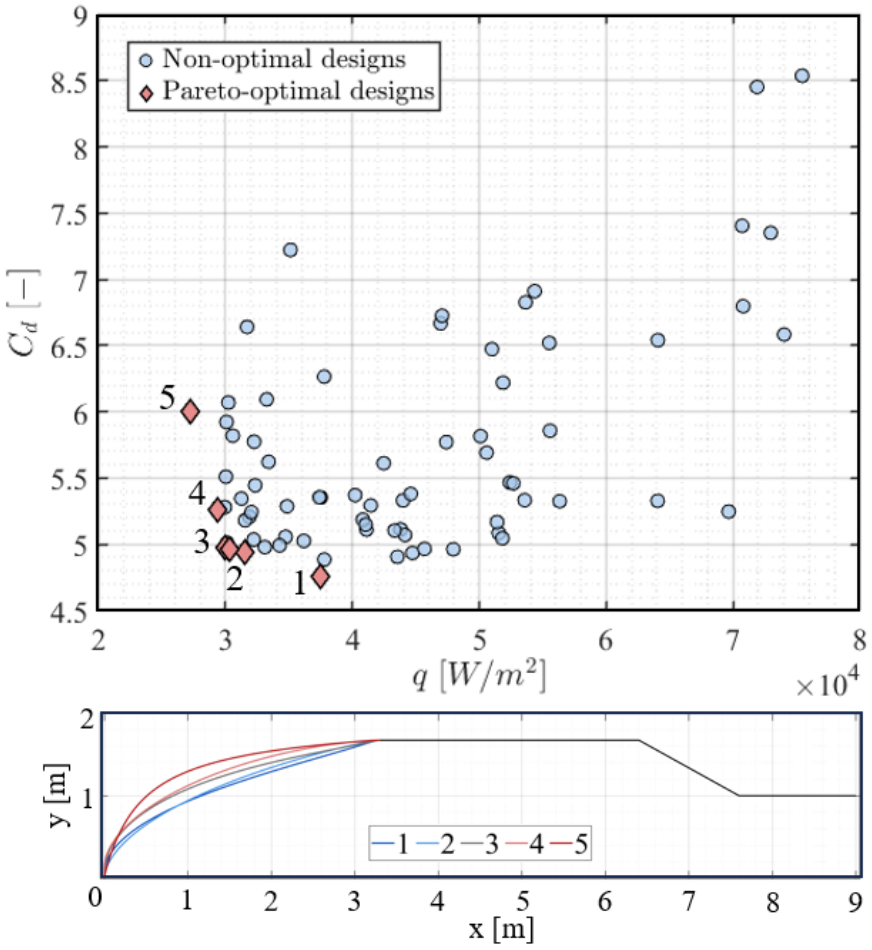


Figure 5 – Overview of the tested fairing shapes for the supersonic case, highlighting Pareto front.

The Pareto front, generated with a total number of 70 simulations, captures the trade-offs between aerodynamic drag and surface heat flux, underlining the conflicting nature of the two objectives. Figure 6 illustrates three of the five configurations belonging to the Pareto front: configuration 1 prioritizes drag reduction, configuration 3 is a compromise between drag and heat flux reduction, while configuration 5 prioritizes heat flux reduction.

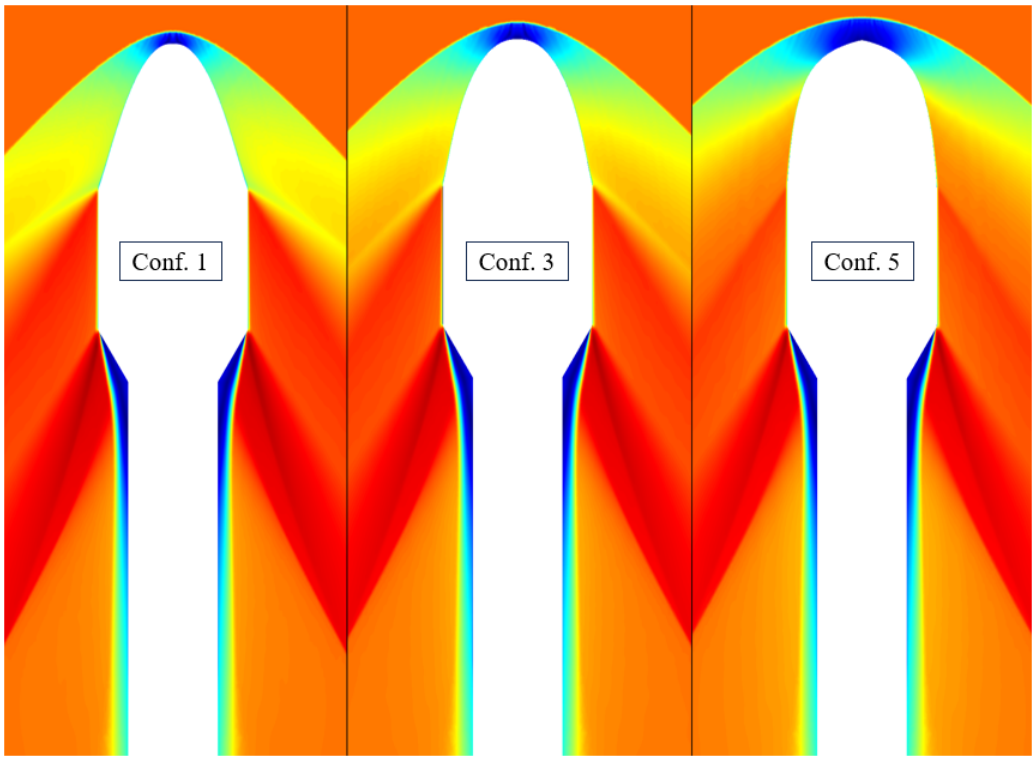


Figure 6 – Supersonic optimal configurations: drag-optimal (left), intermediate trade-off (middle), and heat flux-optimal (right).

The use of narrow and elongated shapes effectively minimizes aerodynamic drag; indeed, such slender geometries promote a weaker shock wave, significantly reducing the drag. However, this approach can lead to severe thermal loads, which can be mitigated by employing a blunter nose. The drag and peak heat flux values for the three selected geometries are summarized in Table 3.

Table 3 – Performance comparison of the selected Pareto front configurations.

Configuration	**Peak Heat Flux [kW/m^2]**	**Drag Coefficient [-]**
1	37	4.76
3	30	4.96
5	27	6.01

The intermediate configuration emerges as a highly effective trade-off between the two competing objectives. When compared to the drag-oriented extreme, this compromise solution achieves a nearly 20% reduction in peak heat flux (from 37 to 30 kW/m^2) at the cost of a mere 4.2% increase in the drag coefficient. Furthermore, when evaluated against the heat flux-oriented design, the intermediate shape incurs only a 10% increase in thermal loads, while providing a substantial aerodynamic advantage by reducing the drag coefficient by 21.17%. Ultimately, this intermediate geometry successfully balances the competing physical effects.

3.3 Cross-regime analysis

In this section, a cross-regime evaluation is performed to provide a broader assessment of the optimized configurations across the full flight envelope. Optimizing the fairing shape for a single flight regime only provides a partial perspective of the aerodynamic problem, since a launch vehicle operates under substantially different flow conditions throughout ascent. For this reason, the configurations identified as optimal for drag minimization in the subsonic ($M = 0.5$), transonic ($M = 0.81$), and supersonic ($M = 1.8$) regimes are evaluated under flow conditions different from those for which they were originally optimized. In addition, for the supersonic regime, the intermediate configuration

extracted from the Pareto front is also included in the analysis, as it represents a balanced trade-off between aerodynamic drag and peak heat flux. This approach makes it possible to analyze how the optimal solutions associated with a specific regime behave when operating outside their original design conditions.

The following figures illustrate the Mach number contours for each simulation, organized by flight regime: all candidate shapes are tested first under subsonic conditions, followed by transonic and supersonic regimes.

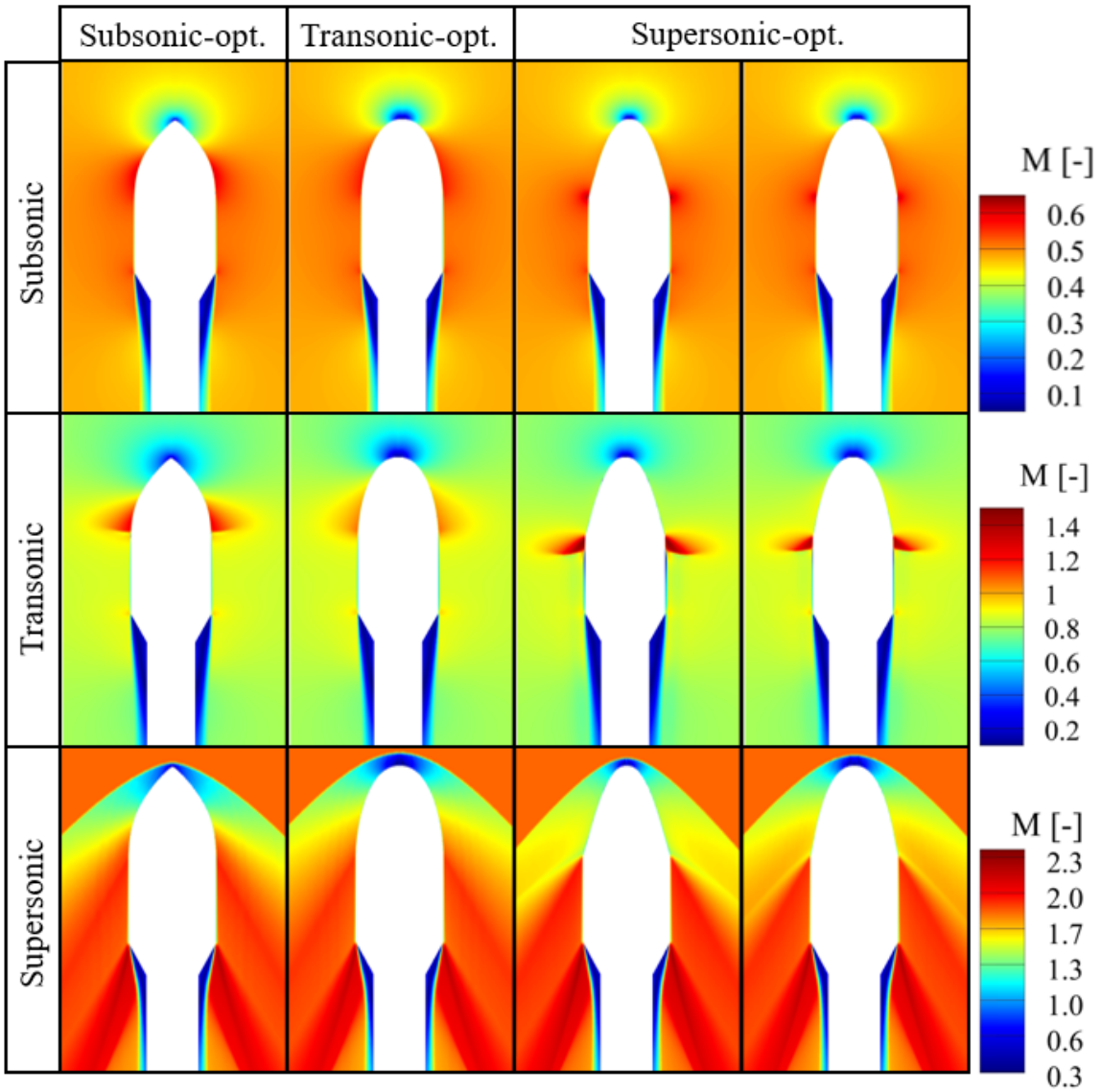


Figure 7 – Cross-regime comparison of Mach number contour fields for the selected optimized configurations. The first and second supersonic configurations correspond respectively to the fully drag-optimized solution and to a compromise solution balancing drag reduction and peak heat flux mitigation.

For each flight regime, the contour plots are arranged from left to right corresponding to the subsonic optimum, transonic optimum, supersonic drag-optimal, and supersonic intermediate configuration, respectively. As observed from Figure 7, transonic optimization favors smooth shape variations able to reduce shock-related drag effects. The transonic optimal shape effectively reduces the flow acceleration along the profile, leading to a shock wave of lower intensity compared to both the subsonic optimum and, more significantly, the supersonic optimum.

It is observed that the supersonic drag-optimal configuration tends to avoid excessively slender shapes. In fact, the presence of a blunter nose induces a more intense flow expansion over the

fairing surface. This contributes to a significant reduction in surface pressure, decreasing the overall aerodynamic drag.
In Table 4, the results in terms of drag coefficient are shown for each simulation.

Table 4 – Cross-regime matrix of drag coefficient values, C_d [-], for the optimized configurations.

	Optimized Configurations			
Flow Regime	**Subsonic**	**Transonic**	**Supersonic (Drag)**	**Supersonic (Interm.)**
Subsonic Regime	1.052	1.056	1.069	1.070
Transonic Regime	1.21	1.17	1.77	1.49
Supersonic Regime	6.26	5.61	4.76	4.96

The first observation that can be derived from the results is that aerodynamic drag in the subsonic regime is only marginally affected by variations in the fairing shape. In fact, there is a negligible percentage difference between the most efficient profile (the subsonic-optimized shape) and the least performing one, which corresponds to the supersonic-optimized configuration. In contrast, more significant percentage variations are observed in the transonic regime. As indicated in Table 4, the transonic-optimized profile achieves the best performance, whereas again the supersonic-optimized shape represents the worst-case scenario. This results in a substantial drag increase of approximately 50% when the supersonic geometry is utilized in transonic conditions. It should also be noted that the supersonic intermediate configuration optimized for both drag and heat flux also demonstrates superior performance in the transonic regime compared to the supersonic drag-optimal shape. The inclusion of thermal objectives favors a slightly blunter nose, mitigating flow acceleration at lower Mach numbers.
These results highlight the limitations of single-point optimization: a geometry that excels in one flow regime may become highly inefficient in others. Consequently, these findings suggest that a robust fairing design requires a trajectory-based optimization approach, accounting for the integrated performance across the entire atmospheric ascent.

4. Conclusion

The proposed optimization framework, which integrates ANSYS Fluent for aerodynamic simulations with the modeFRONTIER optimization platform, was successfully applied to both single-objective and multi-objective optimizations. In the single-objective drag optimizations, the framework highlighted how minimizing aerodynamic resistance requires completely different geometric profiles depending on the flight speed. For the subsonic regime ($M = 0.5$), the algorithm naturally favored a sharp shape. In contrast, the transonic regime ($M = 0.81$) led to a much blunter profile, which is able to prevent excessive flow acceleration and weaken shock waves. When moving to the supersonic regime ($M = 1.8$), the optimization shifted toward an elongated contour to minimize drag; however, the resulting nose was not excessively sharp.
Focusing on the multi-objective supersonic scenario ($M = 1.8$), the framework captured the design trade-off between minimizing aerodynamic drag and mitigating surface heat fluxes, leading to an effective intermediate design able to balance the two competing phenomena.
Additionally, a cross-regime analysis was carried out, revealing that a geometry that excels in one specific flow regime can underperform when tested in conditions it wasn't designed for. This clearly shows that a single-point optimization is not enough, highlighting the need for an approach that accounts for the integrated performance across the entire flight trajectory. In this context, the supersonic intermediate configuration proves to be a more robust compromise, as it successfully balances thermal loads while also mitigating the transonic drag compared to the supersonic drag-optimal shape.
Future works will focus on developing a trajectory-based optimization framework to simultaneously minimize aerodynamic drag and thermal fluxes across the entire flight profile. Furthermore, extending this approach to three-dimensional simulations will be crucial to account for varying angles of attack and non-axisymmetric flow conditions. Additionally, this optimization framework may be integrated into a multidisciplinary optimization environment.

5. Contact Author Email Address

For any questions regarding this work or requests for additional information, please contact the corresponding author at: daniel.palma@uniroma1.it.

6. Copyright Statement

The authors confirm that they, and/or their company or organization, hold copyright on all of the original material included in this paper. The authors also confirm that they have obtained permission, from the copyright holder of any third party material included in this paper, to publish it as part of their paper. The authors confirm that they give permission, or have obtained permission from the copyright holder of this paper, for the publication and distribution of this paper as part of the ICAS proceedings or as individual off-prints from the proceedings.

References

[1] Nassif J, Hoste J.-J. O and Józsa T. I. Multi-point surrogate-based aerodynamic optimisation of a generic hypersonic waverider. *Aerospace Science and Technology*, Vol. 175, Article 111978, 2026.

[2] Kenway G. K. W and Martins J. R. R. A. Multipoint aerodynamic shape optimization investigations of the common research model wing. *AIAA Journal*, Vol. 54, No. 1, pp. 114–128, 2016.

[3] Massaro A, D'Andrea A and Benini E. Multiobjective-multipoint rotor blade optimization in forward flight conditions using surrogate-assisted memetic algorithms. *Proceedings of the 37th European Rotorcraft Forum*, Italy, 2011.

[4] Hicken J. E and Zingg D. W. Induced-drag minimization of nonplanar geometries based on the Euler equations. *AIAA Journal*, Vol. 48, No. 11, pp. 2579–2591, 2010.

[5] Hashimoto A, Jeong S and Obayashi S. Aerodynamic optimization of near-future high-wing aircraft. *Transactions of the Japan Society for Aeronautical and Space Sciences*, Vol. 58, No. 2, pp. 73–82, 2015.

[6] Yu M, Liu J, Huo W and Zhang J. Shape optimization of the streamlined train head for reducing aerodynamic resistance and noise. *Applied Sciences*, Vol. 12, No. 19, Article 10146, 2022.

[7] Colonno M. R and Alonso J. J. The optimum launch vehicle fairing: an MDO approach. *Proceedings of the 12th AIAA/ISSMO Multidisciplinary Analysis and Optimization Conference*, AIAA Paper 2008-5883, 2008.

[8] Sunil K, Johri I and Priyadarshi P. Aerodynamic shape optimization of payload fairing boat tail for various diameter ratios. *Journal of Spacecraft and Rockets*, Vol. 59, No. 4, pp. 1134–1147, 2022.

[9] Yin M, He E, Li Y and Zhang C. Aerodynamic shape optimization of hypersonic vehicle based on improved class-shape-transformation method. *Advances in Space Research*, Vol. 76, No. 11, pp. 5518–5534, 2025.

[10] Shen X, Wang A, Liu W and Wang R. CFD-based aerodynamic optimization of the fairing for a high-speed elevator. *Scientific Reports*, Vol. 15, Article 22243, 2025.

[11] Della Monica M and Bernardini M. Strategies for CFD investigation and optimization of the external aerodynamics of a sounding rocket. *Aerotecnica Missili & Spazio*, 2025.

[12] Samareh J. A. A survey of shape parameterization techniques for multidisciplinary optimization. NASA Langley Research Center, NASA/TM-1999-210100, 1999.

[13] Morita Y, Rezaeiravesh S, Tabatabaei N, Vinuesa R, Fukagata K and Schlatter P. Applying Bayesian optimization with Gaussian process regression to computational fluid dynamics problems. *Journal of Computational Physics*, 2022.

[14] Mahfoze O. A, Moody A, Wynn A, Whalley R. D and Laizet S. Reducing the skin-friction drag of a turbulent boundary-layer flow with low-amplitude wall-normal blowing within a Bayesian optimization framework. *Physical Review Fluids*, 2019.

[15] Meo A, Aponte A, Munafo A, Gori G and Panesi M. A Bayesian framework for the shape optimization of atmospheric reentry vehicles. *Proceedings of the AIAA AVIATION Forum and ASCEND Conference*, 2024.

[16] Talnikar C, Blonigan P, Bodart J and Wang Q. Parallel optimization for LES. *Center for Turbulence Research, Proceedings of the Summer Program*, 2014.

[17] Tian X and Li J. Robust aerodynamic shape optimization using a novel multi-objective evolutionary algorithm coupled with surrogate model. *Structural and Multidisciplinary Optimization*, 2020.

[18] Jones D. R, Schonlau M and Welch W. J. Efficient global optimization of expensive black-box functions. *Journal of Global Optimization*, 1998.

[19] Emmerich M. T. M, Giannakoglou K. C and Naujoks B. Single and multiobjective evolutionary optimization assisted by Gaussian random field metamodels. *IEEE Transactions on Evolutionary Computation*, Vol. 10, No. 4, pp. 421–439, 2006.

[20] McKay M. D, Beckman R. J and Conover W. J. A comparison of three methods for selecting values of input variables in the analysis of output from a computer code. *Technometrics*, Vol. 21, pp. 239–245, 1978.

[21] Menter F. R. Two-equation eddy-viscosity turbulence models for engineering applications. *AIAA Journal*, Vol. 32, No. 8, pp. 1598–1605, 1994.